PAAT

PROGRESS IN AEROSPACE AND AVIATION TECHNOLOGY
e-ISSN: 2821-2924

Vol. 6 No. 1 (2026) 9-22
https://publisher.uthm.edu.my/ojs/index.php/paat

Aerodynamic Study of a Single Groove on the Upper Surface of a NACA 0012 Airfoil at Low Angles of Attack

Wan Muhammad Aqil Wan Nawang[1], Mohd Fauzi Yaakub[1]*

[1] *Faculty of Mechanical and Manufacturing Engineering,*
Universiti Tun Hussein Onn Malaysia, 86400, Johor, MALAYSIA

*Corresponding Author: fauziy@uthm.edu.my
DOI: https://doi.org/10.30880/paat.2026.06.01.002

Article Info

Received: 14 July 2025
Accepted: 1 March 2026
Available online: 30 June 2026

Keywords

Angle of attack, lift, drag, vortex, aerodynamics, groove

Abstract

This study investigates the aerodynamic effects of a single semicircular groove on the upper surface of a NACA 0012 airfoil at low angles of attack (0°–10°) using computational fluid dynamics (CFD) in ANSYS Fluent. The work aims to determine the groove size and chordwise position that enhance lift and reduce drag through passive flow control for UAV and low-speed aerodynamic applications. Three groove diameters (5 mm, 10 mm, and 15 mm) were tested at 25% chord length (0.25c). The 10 mm groove produced the best performance, increasing lift by 3.88% at 6° AoA and reducing drag by 8.84% at 10° AoA relative to the baseline airfoil. The 10 mm groove was then evaluated at chordwise positions of 0.25c, 0.3c, 0.4c, 0.5c, 0.6c, and 0.75c, with the 0.25c position producing the highest lift and the most significant drag reduction. Flow visualization showed that the groove generated a recirculating vortex that energized the boundary layer and delayed flow separation. Validation against the experimental data showed a maximum deviation of 7.26%, supporting the reliability of the two-dimensional CFD model. The study concludes that a properly sized and positioned groove can improve airfoil performance without external energy input, offering practical benefits for aerodynamic design.

1. Introduction

Airfoils are the cross-sectional profiles used in aircraft wings, tails, missile fins, helicopter blades, and wind-turbine blades. Their geometry strongly influences aerodynamic performance because it governs the generation of lift and drag when exposed to an airflow [1], [2]. When an airfoil is placed at a given angle of attack (AoA), pressure and velocity differences develop between the upper and lower surfaces, producing the aerodynamic forces that determine flight performance, maneuverability, and efficiency. Since the early development of powered flight, improvements in airfoil design have therefore remained central to advances in aircraft and rotor-blade performance [1].

Recent aerodynamic research has increasingly examined passive surface modifications, including raised or recessed textures, as a means of improving boundary-layer behavior without requiring external energy input. Numerical and experimental studies on airfoil aerodynamics have shown that surface geometry and operating conditions can significantly influence lift, drag, and flow-separation characteristics [3]-[6]. Such surface features can generate local vortical motion that energizes the near-wall flow, reduces adverse pressure-gradient effects, and delays flow separation. Delayed separation is particularly important because flow separation at higher angles of attack can reduce lift, increase drag, and contribute to stall. Therefore, passive surface modifications have potential benefits for low-speed aircraft, unmanned aerial vehicles (UAVs), and small wind-turbine blades, where aerodynamic efficiency and simplicity are important design considerations.

Although previous studies have investigated surface roughness, vortex generators, dimples, and other passive flow-control devices, the aerodynamic influence of a single semicircular groove on the upper surface of a NACA 0012 airfoil remains less thoroughly documented, especially at low angles of attack. The NACA 0012 airfoil is widely used in aerodynamic studies because of its symmetric geometry and well-established reference behavior [2], [7]. However, small geometric changes on its surface can alter the local flow field and may influence lift and drag in ways that are not immediately apparent from the baseline airfoil geometry.

This study addresses this gap by examining the aerodynamic effects of a single groove on the upper surface of a NACA 0012 airfoil at low angles of attack from 0° to 10°. Using computational fluid dynamics (CFD), which is widely applied for numerical analysis of aerodynamic flows [8], the study evaluates the influence of groove size and chordwise position on lift coefficient, drag coefficient, pressure distribution, and velocity contours. The objectives are to investigate the aerodynamic effect of a single groove at low angles of attack, to assess how groove geometry influences flow separation and aerodynamic performance, and to determine how the groove position on the upper surface affects lift and drag. The findings are intended to support the development of simple passive flow-control strategies for improving airfoil performance in low-speed aerodynamic applications.

2. Methodology

The numerical investigation was conducted through a systematic CFD procedure. The process began by identifying the research problem and defining the simulation parameters, including the airfoil geometry, chord length, groove size, groove position, inlet velocity, angle-of-attack range, and solver settings. A baseline NACA 0012 airfoil was first modeled to establish a reference case. The baseline case was meshed, assigned with appropriate boundary conditions, solved in ANSYS Fluent, and validated against published experimental data before any groove modifications were introduced.

After the baseline model was validated, semicircular grooves of different sizes were introduced on the upper surface of the airfoil to evaluate their influence on lift and drag. The groove size that produced the best aerodynamic response was then retained for a second set of simulations in which the groove was placed at several chordwise positions. For each case, lift and drag coefficients were extracted, and the pressure distribution and velocity contours were analyzed to explain the aerodynamic trends. This workflow ensured that the final comparison was based on a validated baseline and a consistent numerical setup across all configurations.

2.1 Simulation Setup

Table 1 summarizes the main geometrical and operating conditions used in the simulations. The NACA 0012 profile was selected as the baseline airfoil, with a chord length of 1 m. The airfoil was analyzed at angles of attack from 0° to 10° in increments of 2°, allowing the aerodynamic response to be evaluated within the low-angle operating range considered in this study.

Table 1 *Airfoil geometry and simulation angles*

Type of airfoil	NACA 0012
Chord length	1 m
Angle of attack	0°, 2°, 4°, 6°, 8°, and 10°

2.2 Design Geometry

The computational geometry was prepared as a two-dimensional model. NACA 0012 coordinate data were obtained from a standard airfoil-coordinate database, normalized to 1 m chord length, and imported into ANSYS DesignModeler using the 3D Curve tool [9]. The trailing edge was closed to ensure that the airfoil formed a complete profile. A C-type computational domain was then generated around the airfoil, consisting of a 5 m semicircular inlet region upstream and a 10 m rectangular extension downstream. The airfoil was subtracted from the domain using a Boolean operation to create the fluid region. The airfoil orientation was adjusted to simulate the required angles of attack. Finally, the domain was divided using projection and slicing tools to support structured quadrilateral meshing. The resulting computational domain is shown in Fig. 1.

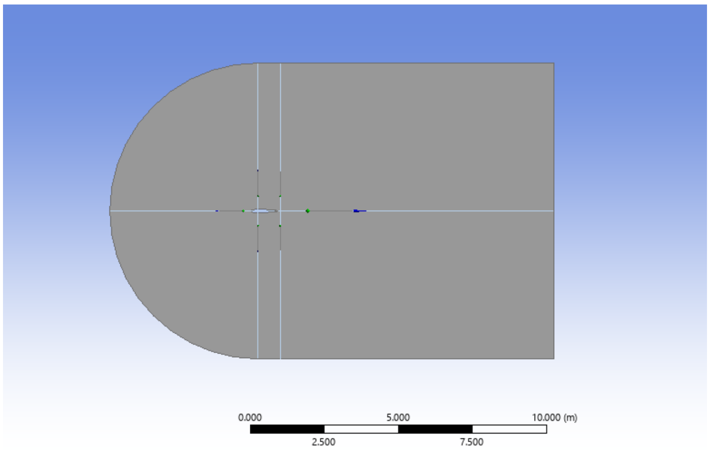

Fig. 1 *Computational fluid domain for the airfoil*

2.3 Meshing

Mesh generation was performed using sizing controls and face meshing. For the baseline airfoil, edge sizing was applied along the airfoil surface, with 200 divisions used to increase the resolution near the wall. For the grooved configurations, inflation layers were added around the groove and airfoil wall to better capture near-wall velocity gradients, recirculation, and boundary-layer behavior. Quadrilateral elements were selected because they provide a structured mesh that is suitable for two-dimensional external aerodynamic simulations. Fig. 2 presents the completed mesh, including the refined region around the airfoil and the surrounding computational domain.

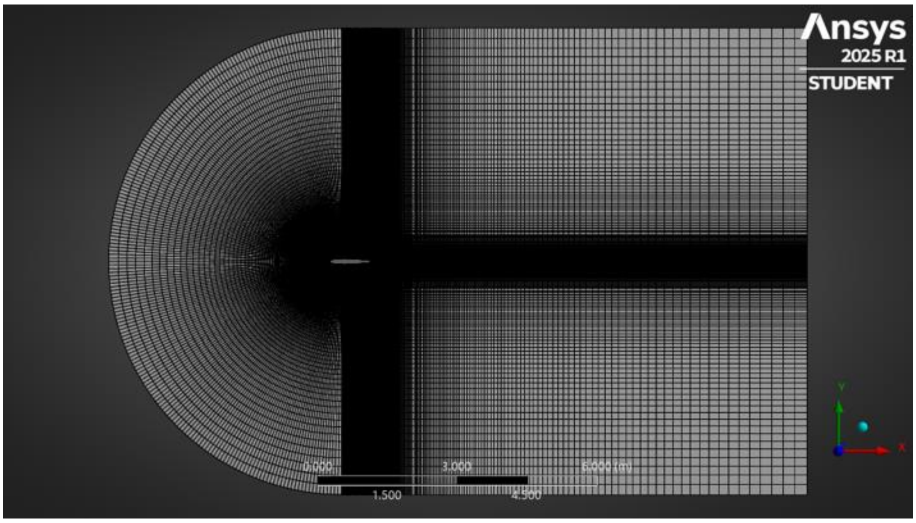

Fig. 2 *Complete mesh of the airfoil computational domain*

2.4 Boundary Setup

The physical models, material properties, and boundary conditions used in ANSYS Fluent are presented in Table 2. A steady, planar, density-based solver was used with the k-omega SST turbulence model to represent the external flow around the airfoil, following established CFD modeling practice for turbulent aerodynamic simulations [8], [10]. Air was defined using a density of 1.225 kg/m3, a specific heat capacity of 1006.43 J/kg-K, a thermal conductivity of 0.0242 W/m-K, and a dynamic viscosity of 1.789×10^{-5} kg/m-s. The inlet was specified as a velocity inlet with a flow speed of 43.9 m/s, while the outlet was defined as a pressure outlet with zero-gauge pressure. The far-field and flow-direction settings were defined consistently so that the incoming flow aligned with the required angle-of-attack condition. These boundary conditions establish the flow environment used to compute the lift and drag coefficients of the airfoil.

Table 2 *Model setup and boundary conditions*

Setup	
Model	k-omega
Solver	Density-based
Velocity formulation	Absolute
Time	Steady
2D space	Planar
Model	
Model	k-omega
	SST
Material selection	
Air	Density = 1.225 kg/m^3
	Specific heat, C_p = 1006.43 J/(kg·K)
	Thermal conductivity = 0.0242 W/(m·K)
	Viscosity = 1.789e-5 kg/(m·s)
Boundary condition	
Far field	Type: pressure far-field
	Gauge pressure = 0 Pa
	Mach number = 0
	x-component of flow direction = 1
	y-component of flow direction = 0
Inlet	Type: velocity inlet
	Velocity specification method = magnitude and direction
	Reference frame = absolute
	Velocity magnitude = 43.9 m/s
	Supersonic/initial gauge pressure = 0 Pa
	x-component of flow direction = 1
	y-component of flow direction = 0
	Turbulence
	Specification method = turbulent viscosity ratio
	Turbulent viscosity ratio = 1
Outlet	Type: pressure outlet
	Gauge pressure = 0 Pa
	Backflow direction specification method = normal to boundary
	Turbulence
	Specification method = turbulent viscosity ratio
	Backflow turbulent viscosity ratio = 1

Table 3 lists the numerical solution methods, initialization procedure, residual monitoring, and force-coefficient monitors used in the simulations. A coupled pressure-velocity scheme with second-order upwind discretization was selected to improve numerical stability and accuracy, consistent with standard finite-volume CFD procedures for external aerodynamic flows [8], [10]. The solution was initialized using the hybrid initialization method, with the inlet used as the reference for the initial flow field. Drag and lift coefficient monitors were created on the airfoil wall, with force vectors defined in the x-direction for drag and the y-direction for lift. The solution was run for 500 iterations for each simulation case, and the aerodynamic coefficients were recorded after convergence of the residual and force monitors.

Table 3 *Solution methods and solver settings*

Solution method	
Model	k-omega
Pressure-velocity coupling	Scheme: coupled
Spatial discretization	
Gradient	Least-squares cell-based
Flow	Second-order upwind
Modified turbulent viscosity	Second-order upwind
Solution control	
Courant number: 5	
Under-relaxation factors:	
Modified turbulent viscosity = 0.75	
Turbulent viscosity = 1	
Solid = 1	
Monitors	
Residual and force monitor	Create: drag coefficient Wall zones: airfoil Option: Print to console and plot Force vector: X = 1, Y = 0 Create: lift coefficient Wall zones: airfoil Option: Print to console and plot Force vector: X = 0, Y = 1
Solution initialization	
Method	Hybrid initialization
Compute from	Inlet
Ref. frame	Relative to cell zone
Initial values	Gauge pressure = 0 Pa x-velocity = 43.9 m/s y-velocity = 0 m/s Temperature = 300 K
Run the calculation.	
Number of iterations = 500	

The same solver configuration was applied consistently to the baseline validation case, the groove-size study, and the groove-position study. This consistency ensured that observed changes in lift, drag, and flow structure were caused by the groove geometry and location rather than by changes in the numerical setup.

3. Results and Discussion

This section presents the numerical results and discusses the aerodynamic behavior of the baseline and grooved NACA 0012 airfoils. The discussion is organized into four parts. First, the grid-independence test is used to verify that the selected mesh provides stable predictions of the lift and drag coefficients. Second, the baseline CFD model is validated against published NACA 0012 experimental data [7] to establish confidence in the simulation procedure. Third, the effects of groove size and chordwise position are evaluated using the computed aerodynamic coefficients. Finally, the pressure-coefficient distribution and velocity contours are examined to explain the flow mechanisms responsible for the observed changes in aerodynamic performance. This structure links the quantitative force-coefficient results with the corresponding flow-field behavior.

3.1 Grid Independence and Validation

A grid independence test was first conducted to ensure that the computed aerodynamic coefficients were not strongly affected by mesh density. This procedure is an important verification step in CFD because numerical solutions should become insensitive to further mesh refinement once adequate spatial resolution has been achieved [8]. The baseline NACA 0012 airfoil was simulated using three meshes containing 60,450, 92,390, and 136,730 nodes. The resulting lift and drag coefficients are shown in Fig. 3, Fig. 4, and Table 4.

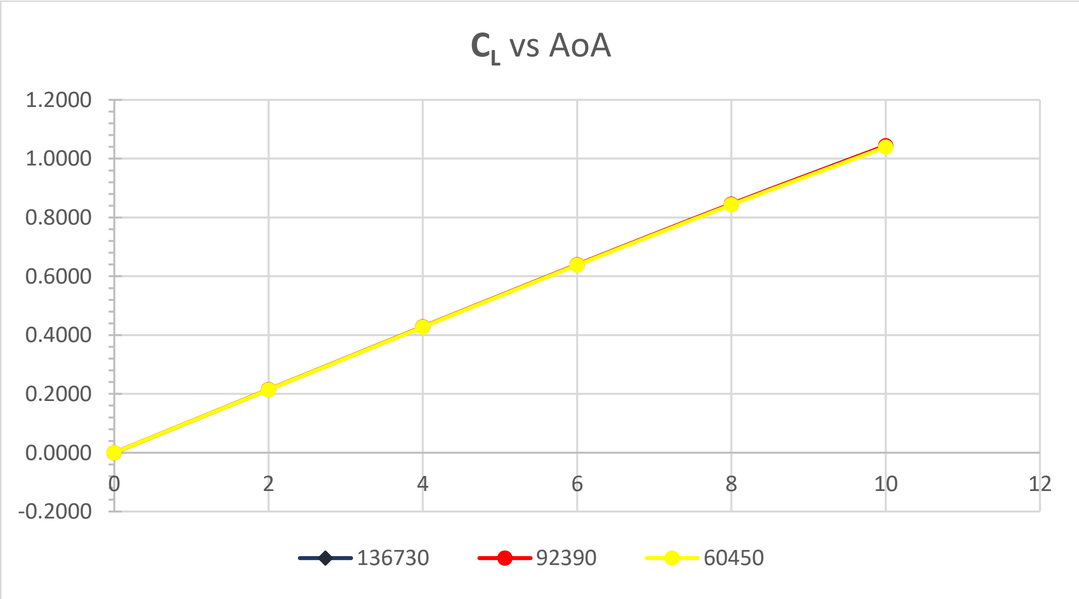

Fig. 3 *Grid independence test for* C_L *versus AoA for the baseline airfoil*

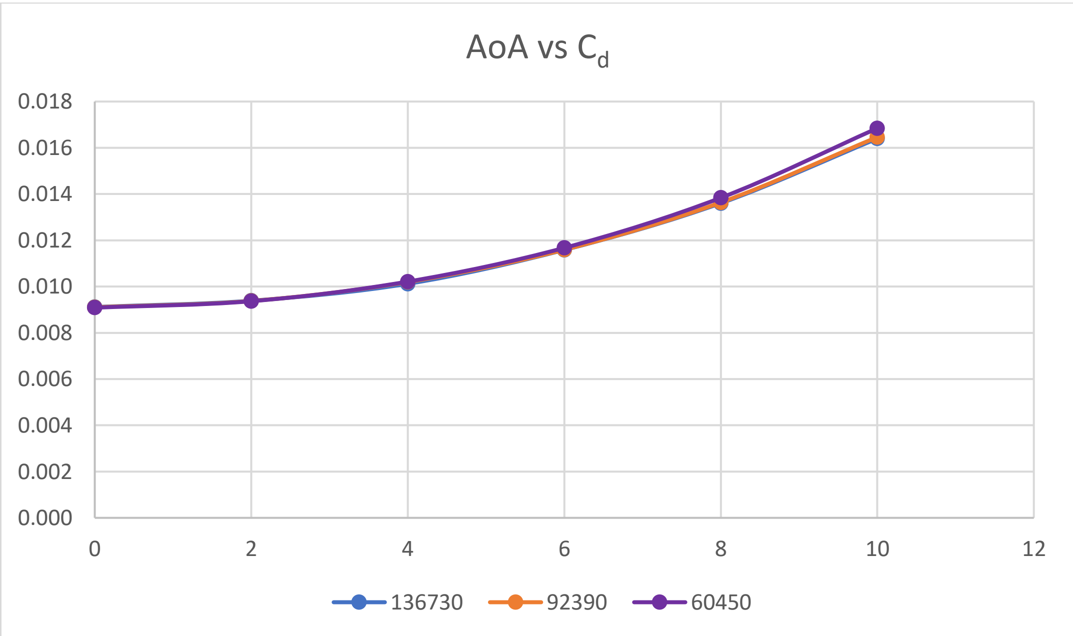

Fig. 4 *Grid independence test for* C_d *versus AoA for the baseline airfoil*

Prog. Aerosp. Aviat. Technol. Vol. 6 No. 1 (2026) p. 9-22

Table 4 *Lift and drag coefficients of the baseline airfoil at different mesh densities*

AOA	Lift coefficient (C_L)			Drag coefficient (C_d)		
	136730	92390	60450	136730	92390	60450
0	0.00000	0.00000	0.00000	0.00912	0.00910	0.00909
2	0.21458	0.21450	0.21415	0.00939	0.00938	0.00937
4	0.42830	0.42819	0.42751	0.01012	0.01020	0.01021
6	0.63951	0.63938	0.63808	0.01158	0.01159	0.01167
8	0.84585	0.84565	0.84320	0.01360	0.01364	0.01384
10	1.04400	1.04360	1.03940	0.01640	0.01646	0.01685

The results in Table 4 show that the lift coefficient varies only slightly among the three meshes at all tested angles of attack. For example, at 10° AoA, $\mathbf{C_L}$ changes from 1.03940 for the 60,450-node mesh to 1.04400 for the 136,730-node mesh. The drag coefficient also shows only minor variation, although the difference is slightly more noticeable at higher AoA. Overall, the close agreement among the three meshes indicates that the solution is sufficiently grid-independent. The 60,450-node mesh was therefore considered adequate for the subsequent simulations because it provides similar accuracy with lower computational cost.

3.1.1 Validation of the Baseline Model

The baseline simulation was validated by comparing the predicted lift coefficient with the experimental data of Abbott and von Doenhoff [7]. The comparison is shown graphically in Fig. 5 and numerically in Table 5. This validation step is important because it verifies that the selected solver settings, computational domain, and mesh resolution can reproduce the known aerodynamic behavior of the NACA 0012 airfoil before the groove modifications are introduced. Fig. 5 and Table 5 show that the simulated lift trend follows the experimental trend over the evaluated range of angles of attack. The experimental values are generally slightly higher than the CFD predictions, which may be due to differences between the idealized two-dimensional numerical model and the physical wind-tunnel conditions, including finite-span effects, surface condition, turbulence level, and measurement uncertainty.

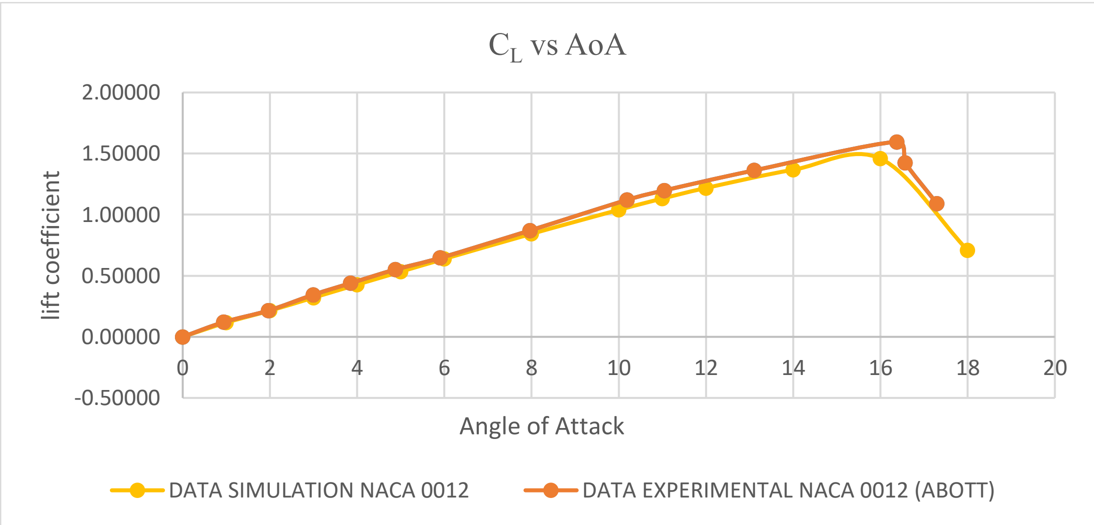

Fig. 5 *Comparison of simulated and experimental C_L values versus AoA*

Table 5 *Experimental and simulated lift coefficients*

No.	Angle of Attack (°)	C_L Experimental, C_{L_e}	C_L Simulation, C_{L_s}	Error	Error Percentage (%)
1	0.00000	0.00000	0.00000	0.00000	0.00%
2	0.94001	0.12061	0.11711	-0.02903	2.90%
3	1.96944	0.21553	0.21415	-0.00641	0.64%
4	2.99515	0.34477	0.32104	-0.06882	6.88%
5	3.85131	0.43960	0.42751	-0.02749	2.75%
6	4.87888	0.55168	0.53330	-0.03332	3.33%
7	5.90831	0.64660	0.63808	-0.01318	1.32%
8	7.96346	0.87076	0.84319	-0.03166	3.17%
9	10.18910	1.12074	1.03937	-0.07261	7.26%
10	11.04710	1.19842	1.13178	-0.05561	5.56%
11	13.10880	1.36252			
12	16.37590	1.59591			
13	16.56780	1.42443	1.45853	0.02394	2.39%
14	17.29710	1.09024			

The percentage error was used to quantify the difference between the simulated and experimental lift coefficients. For this study, deviations below 10% were considered acceptable for validating the two-dimensional CFD model at the investigated low-angle operating range. The percentage error was calculated as follows using the experimental value as the reference:

$$\text{Percentage Error (\%)} = \frac{\left(C_{L_e} - C_{L_s}\right)}{C_{L_e}} \times \mathbf{100}\% \tag{1}$$

The maximum percentage error reported in Table 5 is 7.26%, occurring near 10° AoA. Because all available comparison points remain below the 10% threshold, the baseline CFD setup was considered suitable for evaluating the aerodynamic effects of the groove configurations. The validation also confirms that the model captures the expected lift increase with an angle of attack before the grooved cases are introduced.

3.2 Effect of Groove Size on Aerodynamic Performance

Fig. 6 and Table 6 compare the lift coefficients of the baseline airfoil with those of airfoils containing semicircular grooves of different sizes. For all configurations, C_L increases as the angle of attack increases, which is consistent with the expected lift trend for a symmetric airfoil operating below stall [1], [2]. At low angles of attack, the differences among the baseline and grooved configurations are small, indicating that the grooves have limited influence when the flow remains strongly attached. The 0.01c groove provides the clearest lift improvement at moderate and higher angles of attack. At 6° AoA, C_L increases from 0.63808 for the baseline airfoil to 0.66281 for the 0.01c groove, corresponding to an improvement of approximately 3.88%. The 0.005c groove produces little change, indicating that the groove may be too small to generate a sufficiently strong recirculation effect. In contrast, the 0.015c groove slightly reduces lift in several cases, suggesting that an overly large groove can disturb the upper-surface flow and weaken the lift-generating pressure distribution. These results indicate that the effect of groove size is not linear. A groove that is too small has little aerodynamic influence, whereas a groove that is too large can introduce unnecessary flow disturbance. The 0.01c groove provides the best balance by producing a localized recirculating flow that supports boundary-layer energization without significantly disrupting the main external flow.

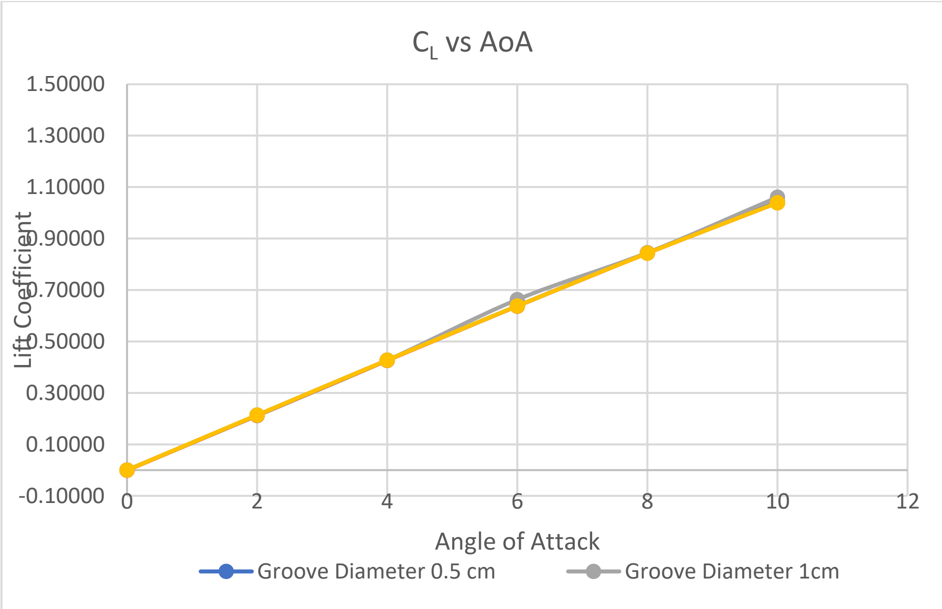

Fig. 6 *Lift coefficient versus angle of attack for different groove sizes*

Table 6 *Lift coefficient for different groove sizes*

	Lift Coefficient			
D/AOA	0.005c	0.01c	0.015c	Baseline
0	-0.00003	0.00022	-0.00116	0.00000
2	0.21373	0.21140	0.21278	0.21415
4	0.42746	0.42690	0.42596	0.42751
6	0.63818	0.66281	0.63706	0.63808
8	0.84450	0.84512	0.84284	0.84319
10	1.04170	1.06077	1.03912	1.03937

The drag results in Fig. 7 and Table 7 show that C_D increases with angle of attack for all groove sizes, as expected due to the stronger adverse pressure gradient and increased flow turning at higher AoA [1], [8]. At lower angles, the differences among the groove configurations are relatively small. However, the effect of groove size becomes more significant at higher AoA. The 0.01c groove produces the lowest drag at 10° AoA, reducing CD from 0.01685 for the baseline airfoil to 0.01536. This represents a drag reduction of approximately 8.84%, indicating that the groove may help delay separation or improve boundary-layer behavior at higher angles of attack. The 0.015c groove, on the other hand, generally increases drag, which supports the observation that an excessively large groove can create additional flow disturbance. Considering both lift and drag, the 0.01c groove was selected for the subsequent chordwise-position study. Taken together, Tables 5 and 6 show that the 0.01c groove gives the most favorable aerodynamic balance. It improves lift at 6° and 10° AoA and reduces drag at 10° AoA, while the smaller and larger grooves provide limited or less favorable benefits. Therefore, the 0.01c groove was used in the next stage to examine the effect of chordwise position.

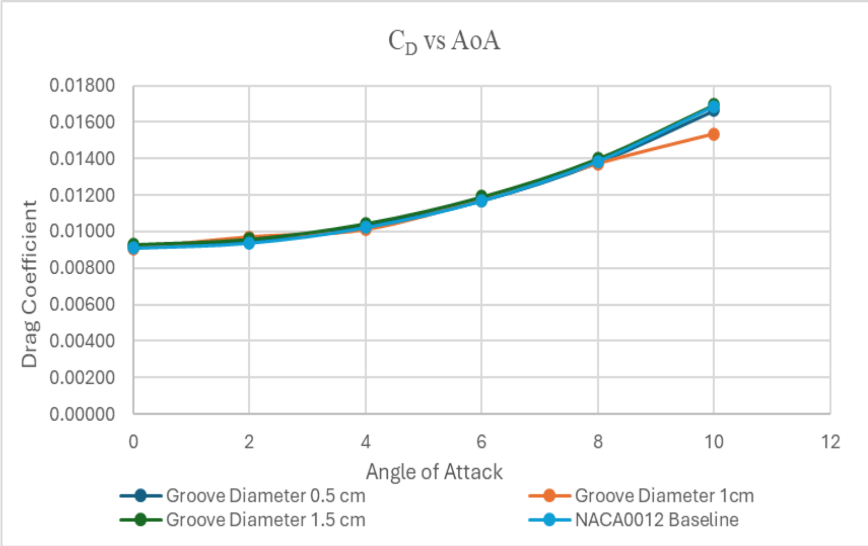

Fig. 7 *Drag coefficient versus angle of attack for different groove sizes*

Table 7 *Drag coefficient for different groove sizes*

	Drag Coefficient			
AoA/Groove size	0.005c	0.01c	0.015c	Baseline
0	0.00916	0.00907	0.00930	0.00909
2	0.00948	0.00970	0.00960	0.00937
4	0.01032	0.01036	0.01045	0.01021
6	0.01170	0.01175	0.01192	0.01167
8	0.01380	0.01373	0.01401	0.01384
10	0.01665	0.01536	0.01696	0.01685

3.3 Effect of Chordwise Groove Position

After identifying 0.01c as the most effective groove size, the groove was placed at several chordwise positions on the upper surface of the airfoil. The positions considered were 0.25c, 0.3c, 0.4c, 0.5c, 0.6c, and 0.75c. Fig. 8 and Fig. 9 show the lift and drag trends, while Tables 8 and 9 provide the corresponding numerical values. The chordwise position of the groove affects the lift characteristics of the symmetric airfoil over the angle-of-attack range from 0° to 10°. At 0° AoA, all positions produce lift values close to zero, which is consistent with the behavior of a symmetric airfoil and indicates that the groove has negligible influence under neutral conditions. At low angles of attack (2°–4°), the 0.3c position produces slightly higher lift than the other positions, although the differences are small. The 0.25c position always gives the most lift at higher angles of attack (6°–10°), with about 3.9% more lift at 6° and 2.0% more lift at 10°. This suggests improved flow attachment and delayed separation when the groove is located closer to the leading edge. As the angle of attack increases from 0° to 10°, the drag coefficient rises for all groove positions. The 0.3c position produces the highest drag at 10° (C_D = 0.01835), whereas the 0.25c position provides the most favorable drag performance. Relative to the baseline, the 0.25c groove reduces drag by 13.45% at 6° and 8.84% at 10°. At lower angles of attack (0°–4°), the differences among the groove positions are small. The pronounced drag reduction at 6° for the 0.25c groove suggests improved boundary-layer behavior, while positions from 0.4c to 0.75c remain close to the baseline response. Overall, the 0.25c groove position provides the best aerodynamic performance because it improves lift and reduces drag at the angles where separation effects become more important. The results suggest that an upstream groove can act as a passive flow-control feature by generating a localized recirculation region that energizes the near-wall flow. For this reason, the 0.25c position was selected as the optimum location for the subsequent pressure and velocity-contour analysis.

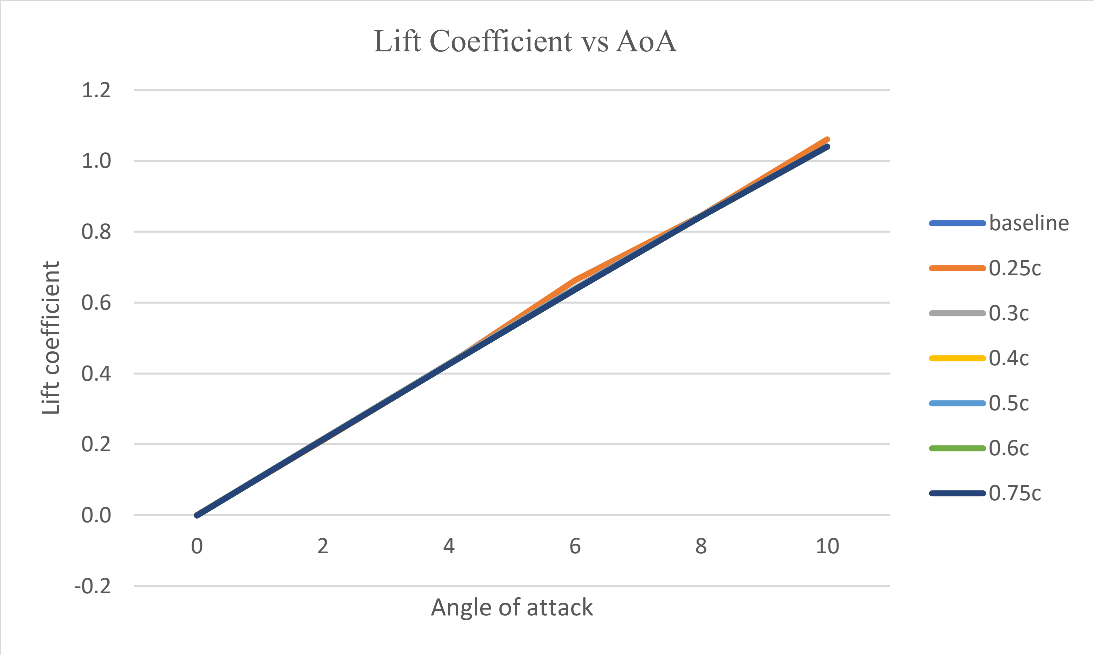

Fig. 8 *Lift coefficient versus angle of attack for different groove positions*

Table 8 *Lift coefficient for different groove positions*

	Lift Coefficient					
AoA/Position	0.25c	0.3c	0.4c	0.5c	0.6c	0.75c
0	0.00022	-0.00063	-0.00028	-0.00035	-0.00123	-0.00099
2	0.21140	0.21435	0.21389	0.21385	0.21303	0.21320
4	0.42690	0.42917	0.42711	0.42686	0.42628	0.42635
6	0.66281	0.64062	0.63770	0.63797	0.63702	0.63705
8	0.84512	0.84495	0.84295	0.84374	0.84284	0.84286
10	1.06077	1.03976	1.04025	1.04077	1.04043	1.04034

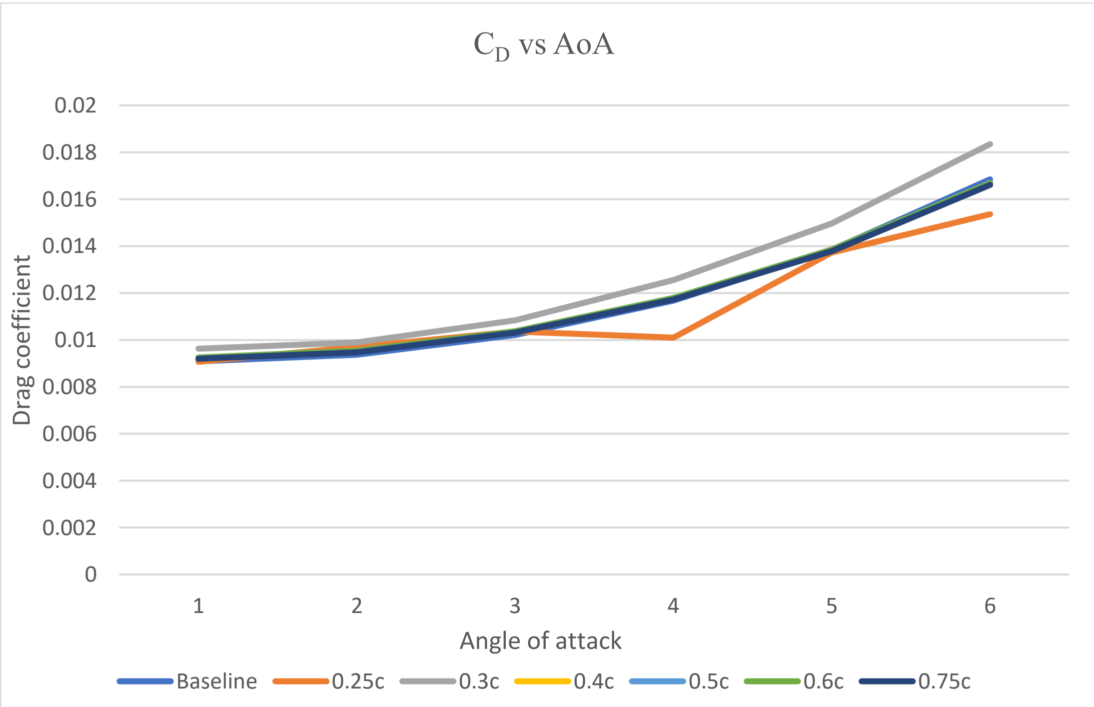

Fig. 9 *Drag coefficient versus angle of attack for different groove positions*

Table 9 *Drag coefficient for different groove positions*

	Drag Coefficient					
AoA	0.25c	0.3c	0.4c	0.5c	0.6c	0.75c
0	0.00907	0.00963	0.00920	0.00922	0.00925	0.00920
2	0.00970	0.00989	0.00949	0.00950	0.00954	0.00948
4	0.01036	0.01084	0.01033	0.01035	0.01038	0.01031
6	0.01010	0.01255	0.01176	0.01178	0.01180	0.01172
8	0.01373	0.01496	0.01383	0.01385	0.01385	0.01378
10	0.01536	0.01835	0.01669	0.01670	0.01668	0.01661

4. Pressure Distribution and Velocity-Contour Analysis

The pressure and velocity fields were examined to explain the aerodynamic trends observed in the lift and drag coefficients. The analysis focuses on the best-performing configuration, namely the 0.01c groove located at 0.25c, and compares its flow behavior with that of the baseline airfoil.

4.1 Pressure-Coefficient Distribution

Fig. 10 presents the pressure-coefficient distribution at 10° AoA for the baseline airfoil and the 0.25c grooved configuration. The grooved airfoil shows sharp local fluctuations in Cp near the groove location, which indicates the presence of a localized vortex or recirculation region inside the groove. This local flow structure helps energize the boundary layer and contributes to delayed separation on the upper surface, consistent with the role of local vortical motion in modifying near-wall flow behavior [8]. The more negative Cp values on the upper surface indicate increased suction, particularly around and downstream of the groove. Because lift is related to the pressure difference between the upper and lower surfaces, the larger separation between the pressure distributions supports the observed increase in lift coefficient at 10° AoA. Thus, the pressure-distribution result confirms that the 0.25c groove contributes to lift enhancement by altering the suction-side pressure field.

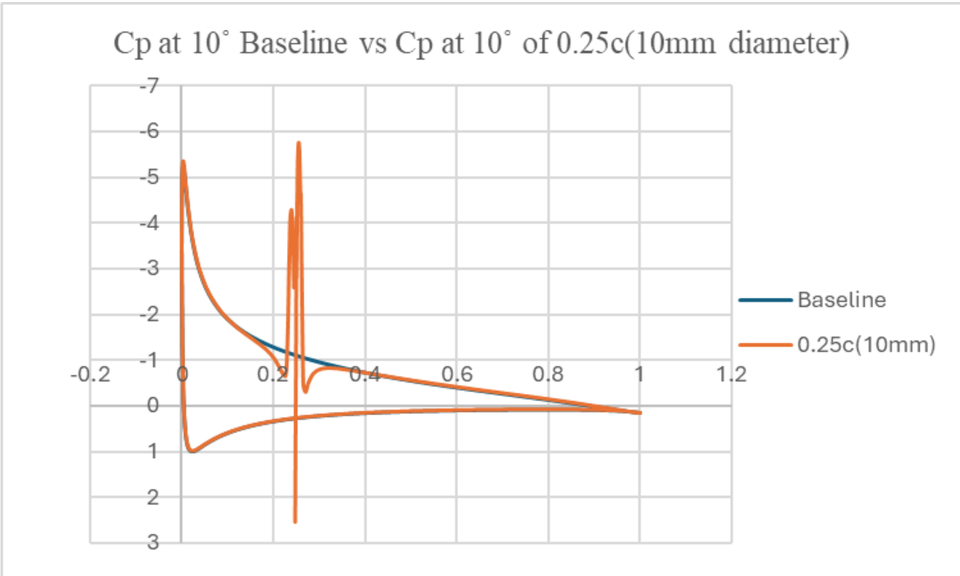

Fig. 10 *Pressure coefficient distribution at 10° AoA*

4.2 Velocity Contour Around the Groove

Fig. 11 shows the velocity contour around the 0.01c groove located at 0.25c. The contour is used to identify the flow behavior inside the groove and to relate the local velocity field to the aerodynamic improvements reported in the coefficient results. The velocity inside the groove is much lower than the free-stream velocity, with values approximately between 0 and 10 m/s. This low-speed region indicates the formation of a recirculation zone within the concave groove. Flow separation is likely to occur near the upstream edge of the groove, followed by reattachment near the downstream edge, forming a closed circulation region. Such a recirculating vortex can interact with the boundary layer above the groove and help maintain flow attachment farther downstream [8]. The velocity contour supports the interpretation obtained from the pressure distribution. The localized low-speed flow within the groove is associated with recirculation, while the higher velocity over the upper surface downstream of the groove contributes to lower suction-side pressure. This pressure reduction increases the lift-generating pressure difference between the upper and lower surfaces. The combined coefficient, pressure, and velocity results therefore show that the 0.01c groove at 0.25c improves aerodynamic performance by modifying the near-wall flow and delaying separation at higher angles of attack.

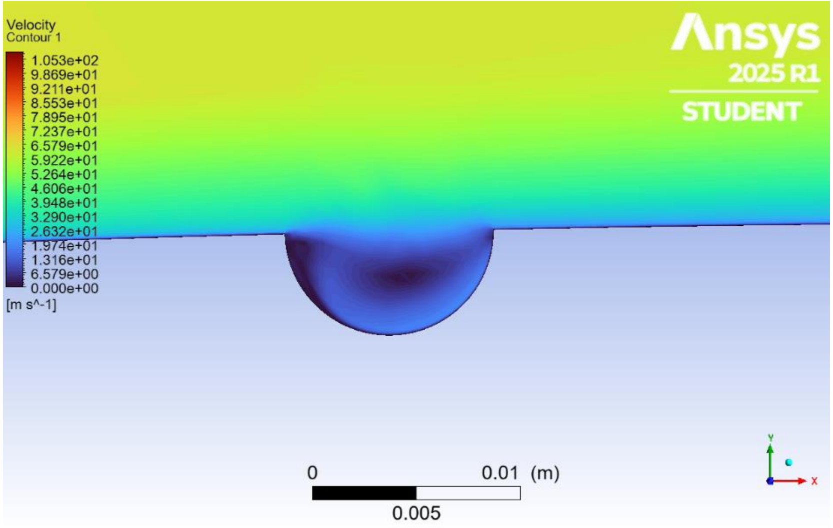

Fig. 11 *Velocity contour around the groove*

5. Conclusion

This study investigated the aerodynamic effects of a single semicircular groove on the upper surface of a NACA 0012 airfoil at low angles of attack. The results show that the 0.01c (10 mm) groove provides the best overall performance among the tested groove sizes, increasing lift by 3.88% at 6° AoA and reducing drag by 8.84% at 10° AoA. The 0.25c chordwise location was identified as the most effective groove position because it improved lift and reduced drag more consistently at higher angles of attack. The pressure and velocity analyses indicate that this improvement is associated with a recirculating vortex inside the groove, which modifies the suction-side pressure distribution and helps energize the boundary layer. The baseline CFD model was validated against experimental lift data, with a maximum deviation of 7.26%, supporting the reliability of the numerical setup. Overall, the findings demonstrate that a properly sized and positioned groove can serve as an effective passive flow-control feature for low-speed aerodynamic applications, including UAVs and small wind turbines.

Acknowledgement

The authors would like to thank the Faculty of Mechanical and Manufacturing Engineering, Universiti Tun Hussein Onn Malaysia, for supporting this research.

Conflict of Interest

Authors declare that there is no conflict of interest regarding the publication of the paper.

Author Contribution

The authors confirm contributions to the paper as follows: ***study conception and design:*** *Wan Muhammad Aqil Wan Nawang, Mohd Fauzi Yaakub;* ***data collection:*** *Wan Muhammad Aqil Wan Nawang;* ***analysis and interpretation of results:*** *Wan Muhammad Aqil Wan Nawang, Mohd Fauzi Yaakub;* ***draft manuscript preparation:*** *Wan Muhammad Aqil Wan Nawang. All authors reviewed the results and approved the final version of the manuscript.*

References

[1] K. Siva Prasad, V. Krishna, and B. Ashok Kumar, "Aerofoil Profile Analysis and Design Optimisation," 2013. [Online]. Available: https://www.researchgate.net/publication/279186627

[2] K. S. Patel, S. B. Patel, U. B. Patel, and A. P. Ahuja, "CFD Analysis of an Aerofoil," 2014. [Online]. Available: www.uvpce.ac.in

[3] A. Nizam Mohammed, M. Anas Mohd Kamil, and O. Jassam Ibrahim, “Numerical Simulation of Airflow Over Three Different Types of Airfoil,” 2019. [Online]. Available: www.fazpublishing.com/aree

[4] S. Soni et al., “Comparative Analysis of Two Airfoils by CFD Simulation,” 2016.

[5] P. Ghose and R. Ranjan, “Effect of Ground Clearance and Air Temperature on Drag and Lift for NACA 2412 Airfoil,” in Advances in Mechanical Engineering, Singapore: Springer, 2021, pp. 177–187, doi: 10.1007/978-981-15-7831-1_17.

[6] M. D. S. H., “A Comparative Flow Analysis of NACA 6409 and NACA 4412 Aerofoil,” International Journal of Research in Engineering and Technology, vol. 03, no. 10, pp. 342–350, Oct. 2014, doi: 10.15623/ijret.2014.0310055.

[7] I. H. Abbott and A. E. von Doenhoff, Theory of Wing Sections: Including a Summary of Airfoil Data. New York, NY, USA: Dover Publications, 1959.

[8] J. D. Anderson, Jr., Computational Fluid Dynamics: The Basics with Applications. New York, NY, USA: McGraw-Hill, 1995.

[9] M. S. Selig, “UIUC Airfoil Coordinates Database,” University of Illinois at Urbana-Champaign. [Online]. Available: https://m-selig.ae.illinois.edu/ads/coord_database.html

[10] ANSYS, Inc., ANSYS Fluent Theory Guide, Release 2025 R1. Canonsburg, PA, USA: ANSYS, Inc., 2025.